

AAPM 2018 // BOOTH #1033



Fully-Automated
TG-142 Tests



One-Click,
Instant Analysis



Full CyberKnife®
TG-135
Machine QA



Full Suite of
Phantom
Analyses



Statistical Tracking &
Trending Database
with RITtrend™



Automated QA
for Helical
TomoTherapy®
TG-148 Tests



Seamless,
Integrated
Patient QA
Workflow



3D Stereotactic
Alignment
Isocenter Analysis



Hancock
MLC Test for
Elekta Machines



**CLICK HERE TO
RESERVE A SPOT**

(Reservation Required)

DON'T MISS THE MOST IMPORTANT MEAL OF AAPM!
THE RIT BREAKFAST SEMINAR
SUNDAY – JULY 29, 2018
7:00–9:00AM AT THE OMNI NASHVILLE HOTEL

The RIT Family of Products:
Medical Physics' Leading QA Software for Over 25 Years

(+1)719-590-1077 • SALES@RADIMAGE.COM

Connect with RIT
[@RIT4QA](https://twitter.com/RIT4QA)



 **RIT**
RADIMAGE.COM

©2018, Radiological Imaging Technology, Inc.
RITrend™ is a trademark of Radiological Imaging Technology, Inc.
CyberKnife® and TomoTherapy® are registered trademarks of Accuray, Inc.

Segmentation of artifacts and anatomy in CT metal artifact reduction

Seemeen Karimi^{a)} and Pamela Cosman

Department of Electrical and Computer Engineering, University of California, San Diego, La Jolla, California 92093

Christoph Wald

Department of Radiology, Lahey Clinic, Burlington, Massachusetts 01805

Harry Martz

Lawrence Livermore National Laboratories, Livermore, California 94551

(Received 25 April 2012; revised 13 August 2012; accepted for publication 14 August 2012; published 11 September 2012)

Purpose: Metal objects present in x-ray computed tomography (CT) scans are accompanied by physical phenomena that render CT projections inconsistent with the linear assumption made for analytical reconstruction. The inconsistencies create artifacts in reconstructed images. Metal artifact reduction algorithms replace the inconsistent projection data passing through metals with estimates of the true underlying projection data, but when the data estimates are inaccurate, secondary artifacts are generated. The secondary artifacts may be as unacceptable as the original metal artifacts; therefore, better projection data estimation is critical. This research uses computer vision techniques to create better estimates of the underlying projection data using observations about the appearance and nature of metal artifacts.

Methods: The authors developed a method of estimating underlying projection data through the use of an intermediate image, called the prior image. This method generates the prior image by segmenting regions of the originally reconstructed image, and discriminating between regions that are likely to be metal artifacts and those that are likely to represent anatomical structures. Regions identified as metal artifact are replaced with a constant soft-tissue value, while structures such as bone or air pockets are preserved. This prior image is reprojected (forward projected), and the reprojections guide the estimation of the underlying projection data using previously published interpolation techniques. The algorithm is tested on head CT test cases containing metal implants and compared against existing methods.

Results: Using the new method of prior image generation on test images, metal artifacts were eliminated or reduced and fewer secondary artifacts were present than with previous methods. The results apply even in the case of multiple metal objects, which is a challenging problem. The authors did not observe secondary artifacts that were comparable to or worse than the original metal artifacts, as sometimes occurred with the other methods. The accuracy of the prior was found to be more critical than the particular interpolation method.

Conclusions: Metals produce predictable artifacts in CT images of the head. Using the new method, metal artifacts can be discriminated from anatomy, and the discrimination can be used to reduce metal artifacts. © 2012 American Association of Physicists in Medicine. [<http://dx.doi.org/10.1118/1.4749931>]

Key words: metal artifact, computed tomography, image segmentation, sinogram in-painting, beam hardening

I. INTRODUCTION

When metal objects are present in x-ray computed tomography (CT) scans, they are accompanied by bright and dark shadows and streaks, collectively called metal artifacts. These artifacts are due to physical processes that cause the assumption of linearity in the reconstruction to break down, so that the scanner projections cannot be accurately reconstructed using filtered backprojection or Radon transform inversion. The artifacts obscure information about anatomical structures, making it difficult for radiologists to correctly interpret the images or for computer programs to analyze them. The problem has existed for many years,^{1,2} and there has been re-

cent progress, but comparisons across different methods have not been made other than with linear interpolation across the metal traces.¹⁻¹³ As a result, there is no robust or widely accepted solution, and it continues to be a challenging research problem.

The separation of artifact from real tissue is not a trivial task. The CT number (voxel intensity) ranges of metal artifacts and anatomical structures overlap, as do their gradient ranges. Metal artifact reduction (MAR) algorithms operate in projection space, so that the scanner projection samples, i. e., measured ray-sums, that do not pass through metal contribute to the final image, along with estimated ray-sums that replace the measured ray-sums passing through the metal. In this

research, we improve upon a class of MAR algorithms based on sinogram in-painting.¹⁻¹³ Sinogram in-painting methods are vulnerable to the misrepresentation of anatomical edges that overlap the metal traces. Various algorithms have tried to address this problem.^{3-8,12,13} We segment regions contaminated by metal artifacts from anatomical structures in the originally reconstructed image, henceforth called the original image. Voxel values in regions affected by artifacts are replaced with values from surrounding regions. Thus, a “prior” image is built. The prior image represents prior knowledge that can be used to guide ray-sum estimation within the metal trace. As in other sinogram in-painting methods, the measured ray-sums outside the traces are left unmodified. The corrected projections are reconstructed to provide the artifact-reduced image.

II. BACKGROUND

II.A. Causes of metal artifacts

Metal artifacts are caused by beam hardening (the preferential attenuation of low energy photons in a polyenergetic x-ray beam), photon scatter, partial volume effects, photon starvation, and data sampling errors. Data sampling errors can be caused by inexact detector or view positions, cone beam effects, or patient motion.¹⁴ Beam hardening and scatter cause low-frequency artifacts, which appear as bright and dark shadows around the metal, obscuring the anatomy actually present in the affected areas. The appearance of these artifacts will be explained in more detail in Sec. III. The other phenomena listed above create high frequency artifacts, namely, streaks. Low frequency artifacts are difficult to remove, but high frequency artifacts can usually be removed by nonlinear filtering.^{15,16}

II.B. Current approaches

Besides sinogram in-painting, other CT reconstruction methods can be used for MAR. Iterative reconstruction algorithms have been used to reconstruct from noise-limited data. These can be adapted for MAR.¹⁷⁻¹⁹ Iterative reconstruction requires accurate modeling of the x-ray generation and attenuation processes in the body and the detector, which is difficult to accomplish. Another drawback of iterative methods is that they are slow because they require repeated reconstructions. Multiple-energy decomposition methods are used to decompose materials into basis materials, and are less susceptible to beam hardening artifacts.^{20,21} Therefore, energy decomposition can be used to reduce metal artifacts.^{12,21,22} Energy decomposition methods take into account the energy-dependent attenuation coefficients of different materials. As a result, they can compensate for artifacts from beam hardening. Two or more x-ray spectra are required for energy decomposition, but multienergy imaging is not standard in clinical scanning protocols, nor does it compensate for scatter. Iterative reconstruction of dual energy data²¹ has the potential to provide excellent images if the dual spectra and models are available. While iterative reconstruction and energy decom-

position based methods have shown good preliminary results, sinogram in-painting is the most practical approach because it is computationally simple, and needs only one energy spectrum. Its most serious challenge is accurate data estimation.

In sinogram in-painting methods, the metal objects are identified in the projection space. The regions in the projection space occupied by the metal are called metal traces. In some methods,¹⁻⁶ metal objects are located in the original image by thresholding, and the traces are located by calculation or reprojection. We use the term scanner projections to denote log-attenuation projections measured from the scanner, or a linearly processed version of them, for example, after rebinning to parallel projections. In other methods,⁷ the metal traces are located directly in the scanner projections. Early work^{1,2} interpolated the scanner projection data on either side of the traces. This method, which we call direct interpolation (DI), misses edges of real structures as shown in Fig. 1. In the picture, a soft tissue background contains a piece of metal and a bony structure. Projections at two angles are shown. In one angle, the bone does not interfere with the metal projection, and the projection can be interpolated without loss of edge information. In the other angle, interpolation of the data would result in an edge being blurred away. The missing edge information results in secondary artifacts in images, which may be as severe as the metal artifacts.

It was proposed that edges be recorded from the original image.³ The edges could be reprojected and combined with the scanner projections to create a smoother projection on which interpolation could be performed. However, a method for recording edge information in reprojections was not defined, but is critical in the performance of a MAR algorithm. It was proposed that the true values of image voxels be estimated using k-means clustering and thresholding.⁵ The reprojections of the estimated voxel values would be used as replacement data in the metal trace. This method was reported to fail when the artifacts were as bright as bone or as dark as air, which occurred in almost all of our test images. Other existing methods built upon the notion of a prior knowledge image that contains edge information.⁶⁻⁸ These methods differ in how they utilize the prior, using various interpolation techniques. One method uses the ratio of scanner projections

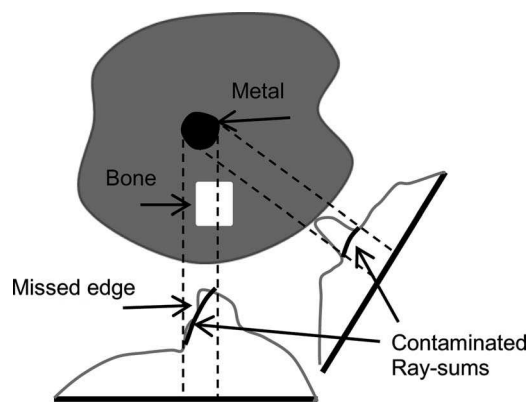


FIG. 1. A schematic of an object and two projections. Direct interpolation results in missed edges in one projection.

to prior reprojections instead of the difference.⁶ Other methods require repeated reconstructions, each of which improves the prior.^{7,8} However, all these methods rely on intensity thresholding to produce the prior image, and intensity thresholding leads to voxel misclassification in the prior. Knowledge of the materials and accurate modeling helps retire some of this risk.¹² Voxel misclassification leads to false edges or missed edges and therefore to secondary artifacts. We call the thresholded-prior methods TP-MAR.⁵⁻⁸ Some TP-MAR methods suggest doing a first pass MAR with DI, and then thresholding this corrected image to create a prior. However, the secondary artifacts from DI-MAR can be intense enough that thresholding still leads to voxel misclassification.

We see that while the notion of the prior image is not new, little attention has been paid to generating an accurate prior image. The sinogram in-painting methods we have mentioned focus on the interpolation technique. Our experiments, described in Secs. V and VI, show that the accuracy of the prior has greater impact on artifact reduction than the particular interpolation technique. There is much room for improvement and for the use of image segmentation, in particular, in the generation of a prior image. Strictly speaking, prior knowledge consists of the observations we make about metal artifacts, but we use the term prior image for a combination of the observations and measured image.

III. SIMULATION STUDY OF METAL ARTIFACTS CAUSED BY BEAM HARDENING

In order to segment areas of artifact and anatomy, we must understand the process of artifact generation. To help us understand the appearance of the metal artifacts, we simulate beam hardening because it leads to low-frequency artifacts. Beam hardening artifacts are similar in appearance to scatter artifacts, which we have not simulated. Subsequently, we will make observations that we use to discriminate between regions of artifact and anatomical structures.

The monoenergetic attenuation process can be described using the Beer-Lambert law.²³ If I_0 is the incident number of photons with energy E_0 , and $\mu(\mathbf{x}, E_0)$ is the linear attenuation coefficient at energy E_0 for the material at some point represented by the vector \mathbf{x} , then the number of photons at the detector is given by

$$I(s, \theta) = I_0 e^{-\int_{s+l\theta \in L} \mu(s+l\theta, E_0) dl}.$$

In the above equation, the integration is done over the scanned space L between source and detector, s is a vector representing the source position, and θ is a unit vector in the direction from the source position to a detector element.

During reconstruction, we reconstruct the log attenuation projections:

$$p(s, \theta) = \int_{s+l\theta \in L} \mu(s+l\theta, E_0) dl = \ln \left(\frac{I_0}{I(s, \theta)} \right).$$

Now, if we have a polyenergetic spectrum S , then the incident number of photons is given by integrating the number of

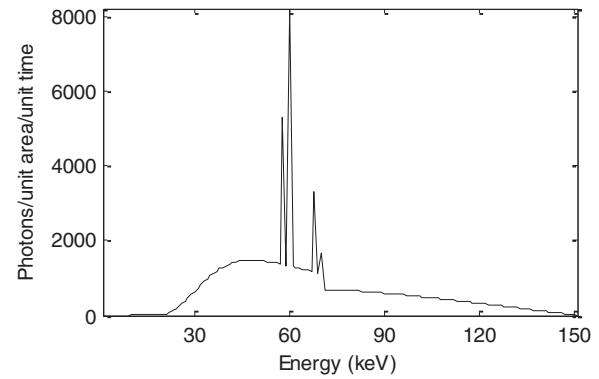


FIG. 2. X-ray spectrum used in beam hardening simulations.

photons at all energies E ,

$$I_0 = \int S(E) dE,$$

and the polyenergetic attenuation process is described as

$$I(s, \theta) = \int S(E) e^{-\int_{s+l\theta \in L} \mu(s+l\theta, E) dl} dE.$$

In this case, the relationship between measured projections p and log-attenuation no longer applies, leading to beam hardening artifacts.²⁴ Compensation for beam hardening due to anatomical tissues is applied during scanner calibration or sometimes in postprocessing.²⁵

We simulate two-dimensional (2D) axial projections of ellipsoids in air of varying eccentricity, using a polyenergetic spectrum. The simulated spectrum is shown in Fig. 2. It was obtained using the program XSPECW2.²⁶ The tube voltage is 150 kVp, the beam filtration is 4 mm of aluminum, and there is a 10° tungsten anode target. The simulated material is iron, whose energy-dependent attenuation cross sections we obtain with XCOM.²⁷ There are 1400 projections, the detector spacing is 0.5 mm at isocenter, and the source-to-isocenter distance is 500 mm. The projections are reconstructed with a Hanning filter with a cutoff of 10 lp/cm. Our image values are clamped between -1024 and 15 383. A monoenergetic simulation was also done for comparison, with a nominal CT value of 30 000 HU (μ corresponding to 80 keV).

While simulations of metal artifacts have been undertaken before,¹⁴ the shape-dependence of the artifacts was not investigated, nor was the accuracy of reprojections through metal. Our simulations, discussed in this section, demonstrate the shape dependence of the beam hardening artifacts, explain their appearance with respect to shape, and show how reprojection through the metal cannot quantify the metal.

Figure 3 illustrates the shape dependence of the beam hardening artifact. When the object cross section is circular, the beam hardening artifact does not exist outside the object. However, beam hardening is visible within the object in the form of cupping. As the object's eccentricity increases, the beam hardening artifact amplitude outside the object increases. The dark artifact is along the long axis of the ellipse, and the bright artifact is along the short axis.

Figure 4 illustrates the formation of the bright and dark parts of the artifact. Ideal (monoenergetic) and hardened

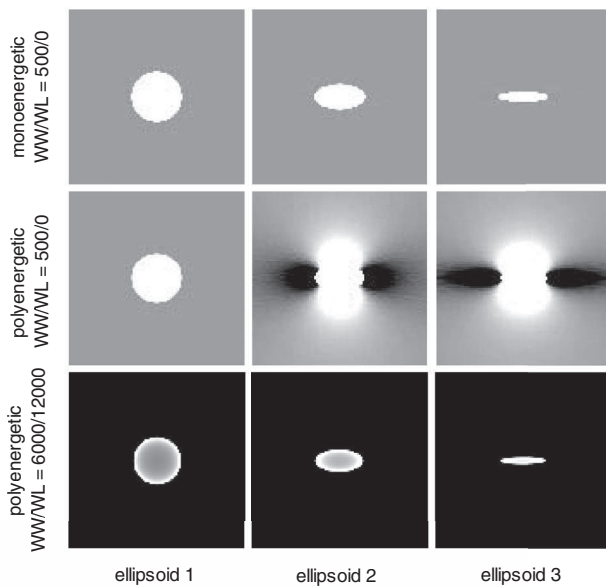


FIG. 3. Illustration of the beam hardening artifact dependence with object shape. The ellipse eccentricity increases from left to right. The top row shows an ideal (monoenergetic) simulation and the bottom two rows show simulated beam hardening. For round objects beam hardening is visible only within the object. This is the well-known cupping artifact. As the metal object eccentricity increases, the artifacts increase as well and are visible outside the object. The dark artifacts are along the long axis (maximum projections). Top two rows: Window Width (WW)/Window Level (WL) = 500/0, bottom row: WW/WL = 6000/12 000 HU.

(polyenergetic) projection data that were filtered with the Ram-Lak kernel are shown next to the image. With a greater ray length through the hardening material, there is a bigger discrepancy between hardened and ideal projections. In the

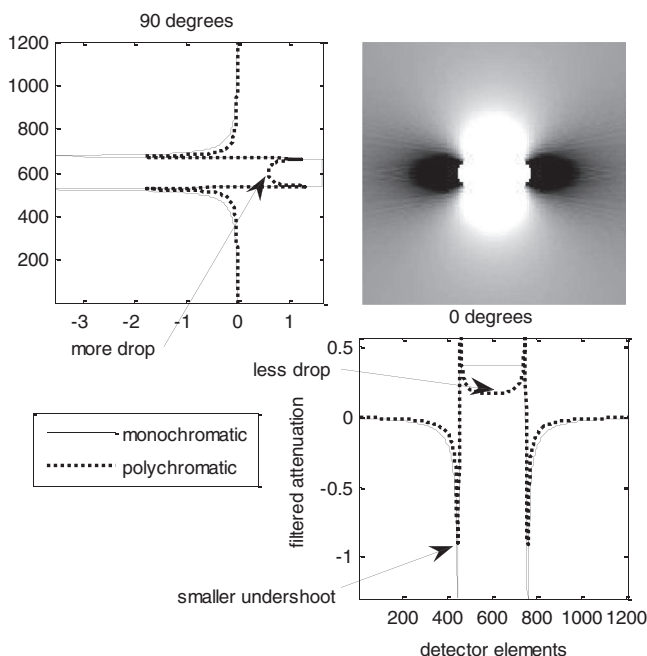


FIG. 4. Illustration of the formation of the beam hardening artifact for a metal object with elliptical cross section. Filtered projections are shown at two angles that correspond to the longest and shortest path lengths through the center of the object.

ideal case, the undershoots of the filtered projection data in all angles perfectly compensate for the metal trace data back-projected across the image. But in the hardened case, there is a distortion of amplitudes. The amplitude of the central ray drops less relative to the ideal in the shorter path (0°) than in the longer path (90°). The undershoots are even smaller along the longer paths relative to the ideal case (due to more hardening) than the shorter paths. This leaves the shorter paths with relatively less negative compensation, leading to the bright artifact, and the longer paths with relatively too much compensation, leading to the dark artifact.

Note that the metal attenuation cannot be quantified by simply reprojecting the metal voxels in a reconstructed image. The hardening of the beam causes overestimation of the reprojections in the direction of highest attenuation, and underestimation in the direction of lowest attenuation. Figure 5 shows that the discrepancy between original hardened projections and reprojections increases with eccentricity. This is because the metal object voxels are reconstructed using projections with different amounts of hardening in each view, but the voxels summed in each reprojected view are the same voxels. Considering the central ray along the long axis, the voxels along it were reconstructed using relatively less-hardened projections along with the more-hardened projections. When compared with the most hardened projections, the reprojections will therefore be greater. A similar reasoning exists for every other ray through the metal. Due to this shape dependence, a simple beam hardening inversion cannot be performed as is done for bone correction in head images in which the skull is roughly ring-shaped in each axial slice.²⁵

We make three observations about metal artifacts in CT images, which are confirmed by the above simulations: the artifacts are adjacent to metal pieces, the amplitude of the artifacts decreases as the distance from the metal increases, and the local maxima through metal in projection space correspond to dark artifacts in the image.

IV. METHOD

Our method to build a prior image operates on the original image. The goal is to discriminate artifacts from real structures in the original image so that we can replace artifact-contaminated regions of the original image with tissue values, thus generating a prior. Our method for segmenting artifacts uses the three observations about metal artifacts given in the previous paragraph. We describe the main concepts in the paragraphs below, and then give details for each step in subsections.

Based on the first observation, local image extrema that are adjacent to the metal voxels and smaller than a given scale are identified and interpreted as metal artifacts. The grouping of voxels for artifact identification (labeling) is done via region growing. The region growing uses a distance-based parameter for voxel inclusion, which makes use of the second observation. The distance-based parameter limits the inclusion of anatomy into the artifact labels. As will be discussed in detail below, these image regions are removed by replacing their voxel values with surrounding voxel values. Also based

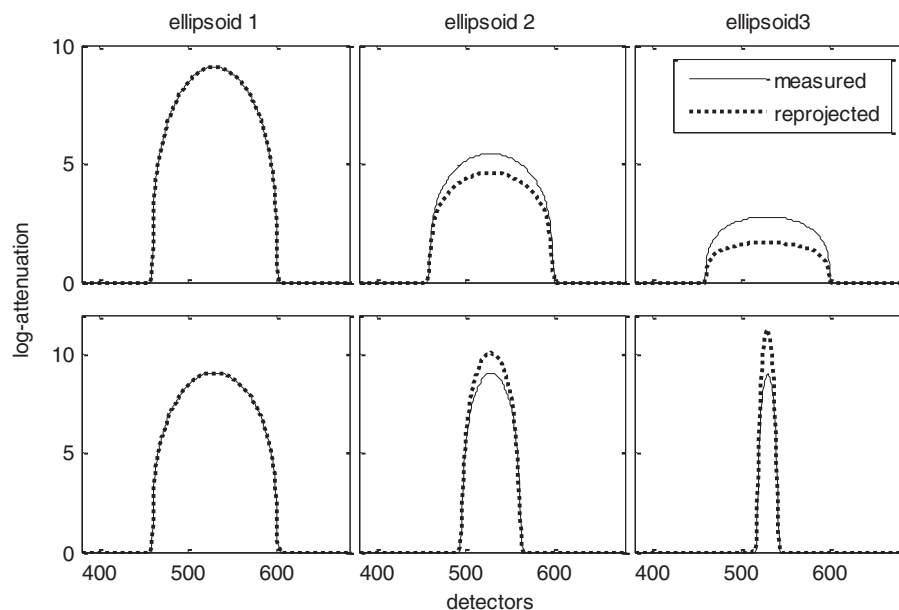


FIG. 5. Reprojections of the thresholded iron ellipsoids shown in Fig. 3 (dotted lines) along with the original hardened projections (solid lines). The top row shows reprojections along the short axis of the ellipsoids, and the bottom along the long axis. Reprojections are underestimated along the short axis and overestimated along the long axis of the ellipsoid.

on the second observation, when a local maximum label contains both artifact and bone, we use a discriminant curve to classify voxels within it as belonging either to artifact or to bone. We restore the bone voxels to the image. Based on the third observation, when a local maximum through metal is found in projection space, we can expect to find local image minima corresponding to it. As a result, we can interpret image minima as artifacts even when they are split off from the metal. The dark artifacts can split off from the metal in the presence of high density CT objects, or multiple pieces of metal. The approach, implemented in MATLAB version 7.10 (The MathWorks Inc., Natick, MA), has the following steps. Figure 6 shows intermediate outputs.

IV.A. Segmentation of metal

Metal voxels are segmented by region growing. Seeds for region growing are voxels above 7000 Hounsfield units (HU). Neighboring voxels are successively added to the region if they are above 3000 HU. Teeth, which have the highest CT intensities for human tissue, are usually less than 3000 HU, so anatomy is not included in metal labels. Labels are generated for each connected metal region.

We then contour the anatomy to prevent dark artifacts from blending into the surrounding air. Figure 6(a) shows the contour by a dotted line. If dark artifacts blended into the surrounding air (as shown in the rectangle), they would not be interpreted as local minima. The contouring method we used is described in Appendix A.

IV.B. Removal of local maxima and minima

Metal artifacts create local maxima and minima around the metal. The removal of maxima and minima are, respectively, performed using closing-by-reconstruction (CBR) fol-

lowed by opening-by-reconstruction (OBR).²⁸ CBR is a morphological operation that performs grayscale dilation with a structuring element followed by iterative erosion that is constrained by the original image. Similarly, OBR first performs grayscale erosion followed by iterations of dilation constrained by the original image. CBR eliminates dark regions (local image minima), and OBR eliminates bright regions (local image maxima) that are smaller than the scale determined by the structuring element. Larger extrema or regions without extrema are left alone. CBR and OBR, respectively, replace voxel values in the closed or opened regions with values derived from voxels surrounding these regions. The structuring element should be at least twice as large as any metal piece in the image to use replacement values outside the artifacts. In order to prevent a too-large structuring element from flooding a local minimum with diffuse bright artifact values, we recommend clamping the image at a high soft tissue value (100 HU) and restoring the image values after CBR.

The OBR and CBR operations will also remove anatomical structures that are smaller than the scale of the structuring element. Figure 6(b) shows the result of OBR and CBR, where anatomical structures have been eliminated along with artifacts. We restore the anatomical structures to the prior by using the following steps to discriminate between anatomy and artifacts.

IV.C. Recovery of nonadjacent anatomical structures

The OBR and CBR processed image is subtracted from the original image. In this difference image [shown in Fig. 6(c)], small intensity differences, attributed to noise or artifact, are eliminated by thresholding. We used a threshold of three times the image noise, which was about 20 HU for our head images.

Next, the positive and negative differences are considered separately. Region growing is performed on the negative

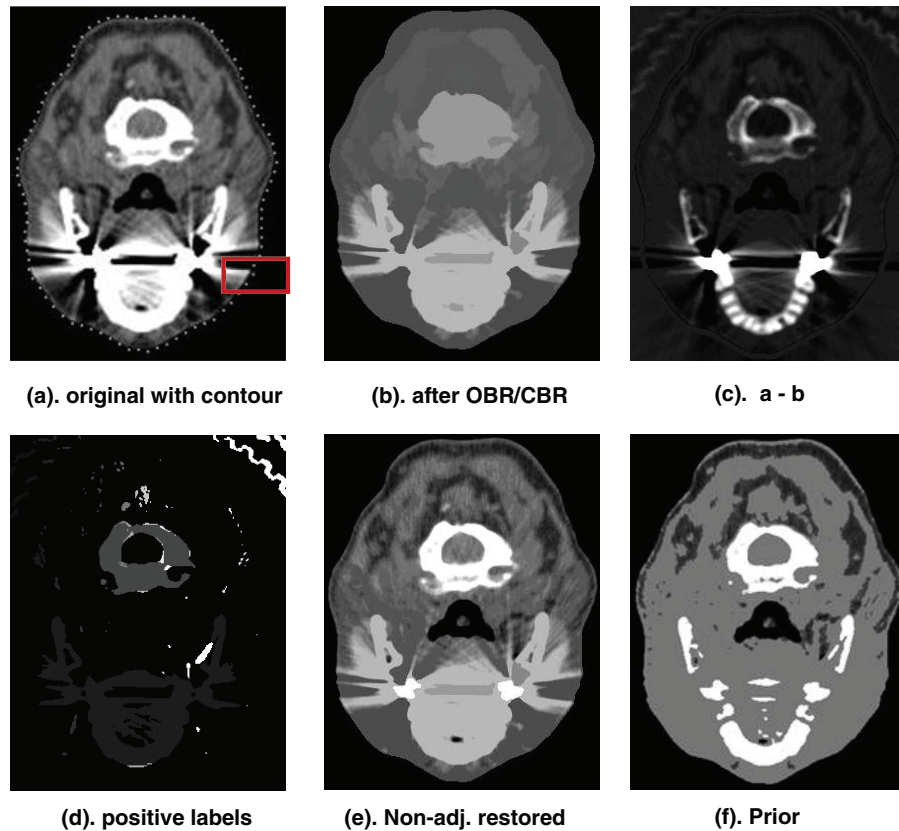


FIG. 6. Stages in the generation of a prior image of a CT head scan. The contour is represented by the dotted line in (a), the image after CBR and OBR in (b), the difference image (a-b) in (c), labels from the positive differences are in (d), the recovery of nonadjacent labels is shown in (e), and the final prior image is in (f). WW/WL = 200/0 HU in (a), (b), (e), and (f). WW/WL 200/-1000 HU in (c).

voxels of the difference image, using an intervoxel intensity threshold that depends on distance from the metal. The justification for a distance-dependent threshold is our second observation, from which we infer that intervoxel variations in artifacts decrease as distance from the metal increases. The distance-dependent threshold limits the grouping of artifacts with anatomy. We generate a distance transform of the image, which is the smallest distance from each voxel to any metal voxel. Our distance-dependent threshold is defined as a function of the distance transform as

$$T_{\delta}(x) = \max(Te^{-aD(x)}, T_{\min}),$$

where $D(x)$ is the value of the distance transform at location x , and T , T_{\min} , and a are constants. We choose T to be 5000 HU to accommodate the large variations in or near the metal, $a = 0.05$, and $T_{\min} = 100$. All values were determined empirically, but are not critical as shown by experiments (varying a from 0 to 0.2) and T_{\min} between 50 and 200 HU.

Similarly, region growing is performed on the positive differences. We use the same equation and parameters for region growing of the positive voxels. From region growing, we get labels of positive or negative polarity. For example, positive polarity labels are shown in Fig. 6(d).

If the labeled regions are not in the neighborhood of a metal label, they are interpreted as anatomical structures, and the voxel values of the original image are restored in those regions. Figure 6(e) shows the recovery of labeled regions that

are not neighboring the metals. The artifact labels may border metal pieces or be separated by interference patterns. We define a neighborhood size of 10 mm.

IV.D. Recovery of adjacent anatomical structures

If a region of positive artifact grows into bone, voxels containing bone would be included in the labeled region and incorrectly replaced with soft tissue values. We exploit the observation that artifact amplitude drops as a function of distance from metal. In the positive labeled regions that remain after the recovery of nonadjacent labels, voxel values of the original image are plotted against the distance transform values. Figure 7(a) shows an example plot. The artifacts generate a cluster in the plot. To separate the artifact cluster from nonartifact voxels, a set of exponential curves is generated with different parameters. The equation for the family of curves is

$$I_c(D) = (I_{\max} - I_{\min})e^{-cD} + I_{\min},$$

where c is the curve parameter, I_{\max} is the maximum value in the region, and D is the distance (distance-transform value). I_{\min} is the minimum of the region values and an outlier bound of 200 HU. The outlier bound value was chosen because the minimum CT number within the artifact cluster was always about 200 HU in our test cases. In any case, lower artifact intensities are removed in a subsequent step. We used no outlier bounds for the upper CT value.

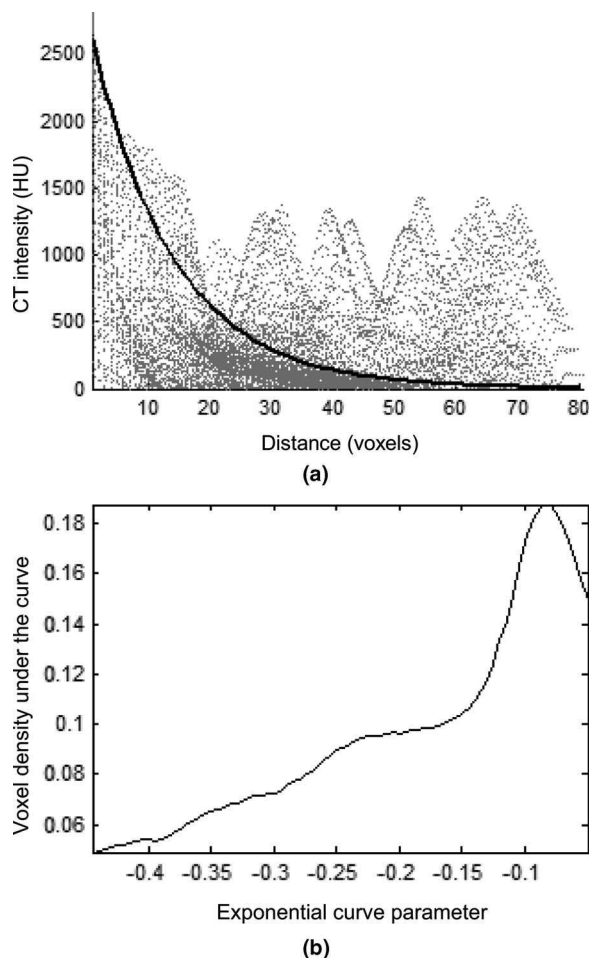


FIG. 7. The relationship between the image intensity and the distance transform for the image in Fig. 6 is shown in (a). The line shows the exponential curve with the best separation of artifact from anatomy. The number of points under each exponential curve, normalized by the area under the curve is shown in (b).

For each curve, the number of voxels under that curve is normalized by the area under the curve. The normalized number of voxels drops past the curve that includes the cluster [Fig. 7(b)]. We choose a curve that is past the peak, to ensure we have captured the cluster, even at the expense of some anatomy. Voxels above this curve are recovered because they are more influenced by anatomy than artifact.

In order to determine whether artifact has indeed grown into anatomy, we compute from the intensity-distance plot, the highest CT value at each distance. We use distance bins of 1 mm. Then we compute the skewness of the resulting distribution. If the skewness is less than 0.15, we assumed that these labels must have grown into bone. The skewness threshold was selected because in our images, the skewness values were about 0.3 in images where the artifact did not grow into bone, and from -0.1 to 0.1 when it did.

IV.E. Deletion of dark artifacts

The local maxima of the projection data are located and matched with negative labels. From Sec. III, we have seen that the local maxima in projection space correspond to dark artifacts in the image. We compute centroids and eigenvectors of

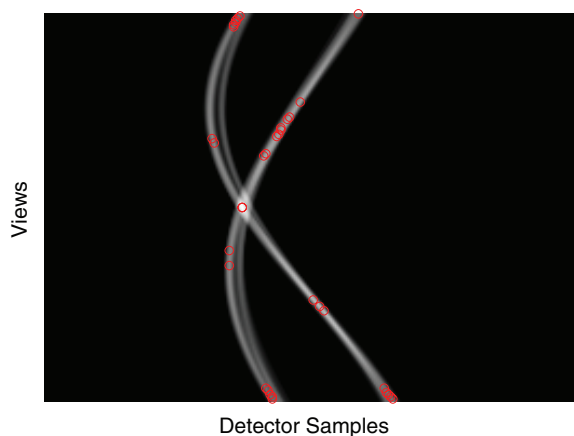


FIG. 8. Reprojections through metal voxels. The local maxima are shown by red circles.

negative labels. For each negative label, we reproject its centroid in the direction of its largest eigenvector. If the centroid projects onto a point that is in the neighborhood of the local maximum of the metal trace, then the label is considered an artifact. We have used a neighborhood size of 10° and 5 mm.

To determine the local maxima in projection space, we reproject only the metal. Figure 8 shows the metal traces. In each projection view, we find the maxima in the sample direction. There are one or more maxima in each view. For each trace and for each view, we extract the local maxima values. We fit a sliding polynomial to the local maxima values extracted at each view. Then we locate the maxima of the fitted curve. The sliding polynomial reduces spurious maxima which may appear due to noise or sampling errors.

We do not use the correspondence of each negative label with a local maximum in projections as a requirement for classifying that label as an artifact, because with multiple projection maxima, negative regions may be combined by region growing. However, the step allows us to add the negative labels that have broken off from the metal. We cannot apply this rule for the bright artifacts (image local maxima), because they do not correspond to local maxima in projection space, rather, they correspond to regions between the local maxima, and are more diffuse in appearance than the dark artifacts.

The processed image created thus far is thresholded by the method in Appendix B. The segmented metal voxels are restored, because each metal piece is a real structure, not an artifact. This completes the generation of the prior image, shown in Fig. 6(f). This prior is reprojected, and the reprojections are used in interpolation, as described in Appendix C.

V. RESULTS

Our method was tested on axial head CT scans. Figures 9 and 10 each show four sets of images with metal artifacts produced from metal coils in cerebral aneurysms, from a deep brain stimulator, and from dental fillings. The original images and images corrected by our MAR algorithm are shown. For comparison, results are also shown for DIMAR (i. e., no prior) and an exemplified TP-MAR (i. e., a

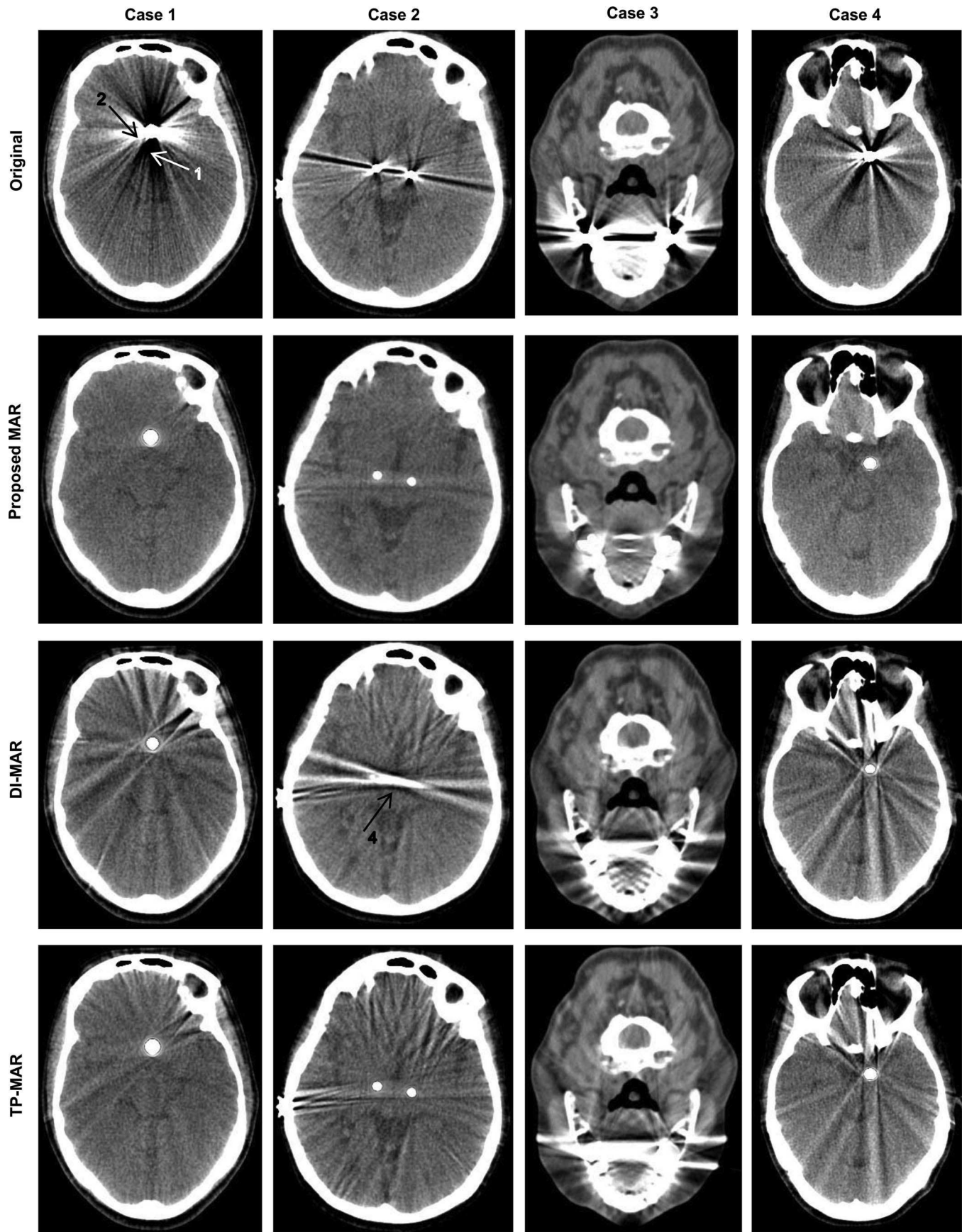


FIG. 9. Four sets of images are shown in columns. Each set contains the original, the proposed method, DI-MAR, and TP-MAR corrected images. In all cases, the proposed prior results in improvements over the original image, over DI, and over TP-MAR. WW/WL = 200/40 HU for cases 1, 2, and 4, and = 500/0 HU for case 3. The arrows point to examples we discuss in the text.

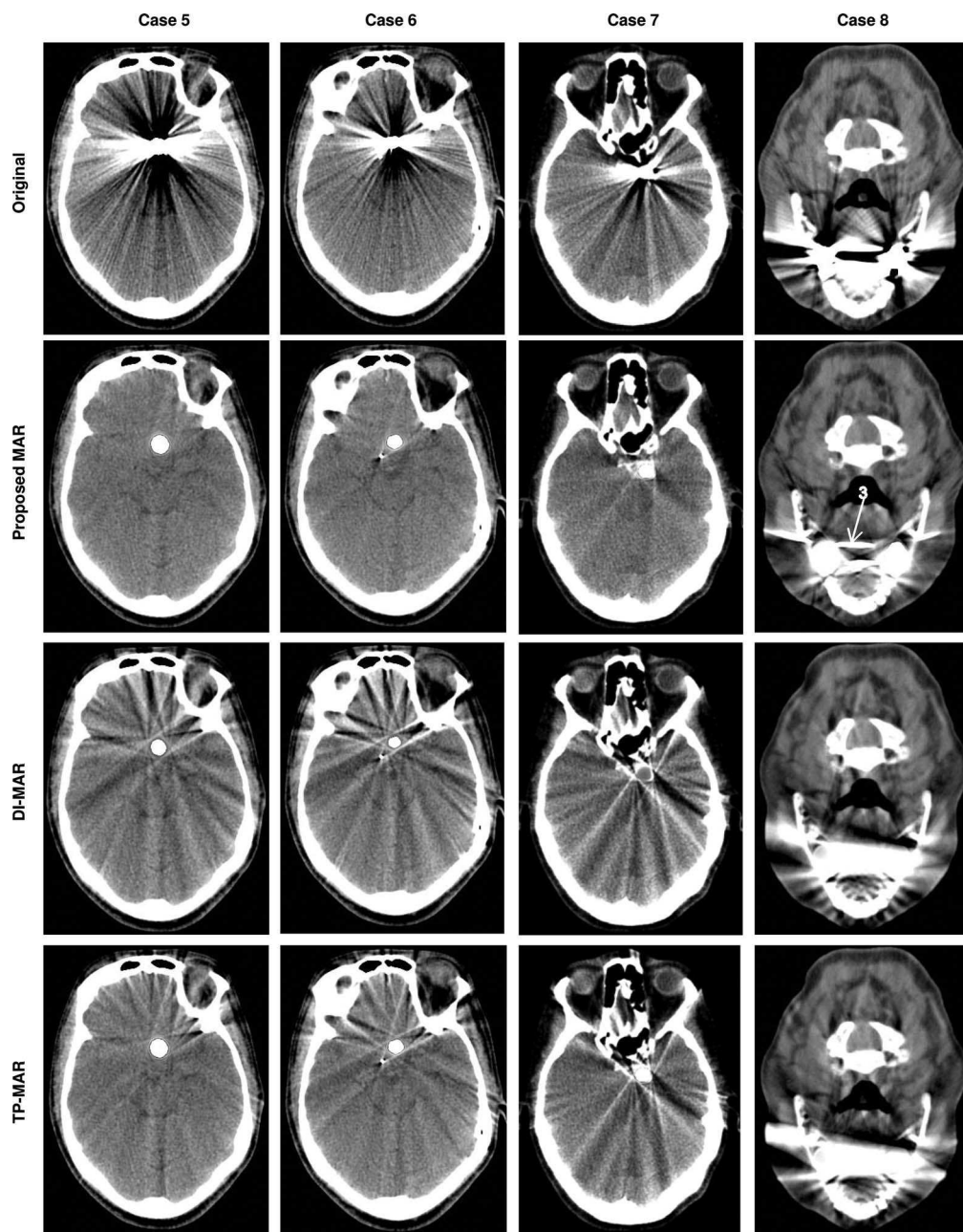


FIG. 10. Another four examples are shown. WW/WL = 200/40 HU for cases 5–7 and 500/40 HU for case 8.

thresholded prior, using the same interpolation described in Appendix C). To generate the TP-MAR prior, we have thresholded the DI-MAR corrected image. Although TP-MAR algorithms vary, we used CT number values recommended in Refs. 5 and 6 for threshold values. Then we used the difference interpolation method for data replacement in the metal traces. In the case of DI-MAR, the metal piece was added back to the corrected image. Since the interpolation technique was the same for all the MAR algorithms, the prior image determined the improvement.

Artifacts are removed by our algorithm even for multiple metal pieces, and from large metal pieces which produce dark artifacts below -1000 HU (arrow 1), and bright artifacts with the CT intensity of bone or cartilage (arrow 2). There were fewer secondary artifacts with our method than the others.

There are residual artifacts in the dental images, especially in Fig. 10 (arrow 3), resulting from the imperfect separation of the artifact from teeth. DI-MAR produces secondary artifacts comparable to the original metal artifacts. The TP-MAR images are better than DI-MAR but not as good as those with our prior.

VI. DISCUSSION

VI.A. Analysis of results

Our algorithm preserves anatomical structures in the prior image, which is why secondary artifacts are reduced. DI-MAR loses edge information in the metal traces, so estimated data are inconsistent with the rest of the sinogram and secondary artifacts are generated, as shown by arrow 4 in Fig. 9.

TP-MAR also loses edge information as described later, but to a smaller extent than DI-MAR.

Our method operates at a region level while TP-MAR methods operate at a voxel level. A region is more informative than a voxel in distinguishing artifacts from anatomy because the region can be examined against more criteria than thresholds. We identify a region with constant polarity, and test if the region or a part of it fits the criteria for artifacts. Considering the positive regions, we use the intensity/distance relationship (observation 2) to separate bone from bright artifacts. Negative regions can be matched with local maxima in the Radon transform (observation 3) to identify them as artifacts.

A TP-MAR prior is generated by thresholding an image into air, soft tissue, or bone. With misclassification of artifact voxels as bone or air, large errors may be produced in the final corrected image, especially when the ratio interpolation (discussed below) is used. Therefore, some TP-MAR methods recommend a first-pass DI-MAR to provide an image with smaller amplitude artifacts, so that thresholding of this corrected image is more likely to create a good prior. However, our experiments show that the secondary artifacts with DI-MAR may be comparable to or worse than the original metal artifacts. Using poor quality DI-MAR images yields poor priors. In the deep-brain stimulator case with multiple metals (Fig. 9, case 2), the DI-MAR secondary artifacts are worse than the metal artifacts in the original image (arrow 4). This leads to a prior that is worse than the prior from thresholding the original image. In the dental cases (cases 4 and 8), the secondary artifacts are misclassified as anatomical structures by thresholding, and preserved or enhanced in the final TP-MAR corrected image.

Figure 11 shows the different priors responsible for the image quality in case 4. The original image is corrected with DI-MAR. The DI-MAR image is then thresholded to produce a TP-MAR prior. Note the partial loss of bone and air pocket structures in the thresholded prior (arrow 5), and better preservation in the proposed prior. The partial loss is why the image quality of the TP-MAR image is in between that of DI-MAR and our method. The DI-MAR algorithm itself results in the

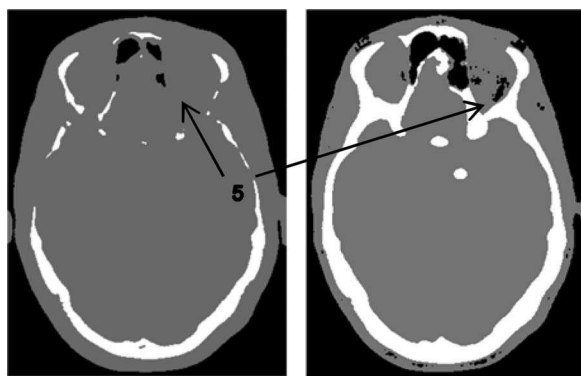


FIG. 11. Priors corresponding to case 4. The left image shows the TP-MAR prior, created by thresholding the DI-MAR image (Fig. 9, row 3). The loss of anatomical edges near the metal leads to a final TP-MAR image that is not much better than DI-MAR in this example. This is because both DI-MAR and TP-MAR have missed nearly the same structures. The right image is the proposed prior, and preserves more of the anatomical structure.

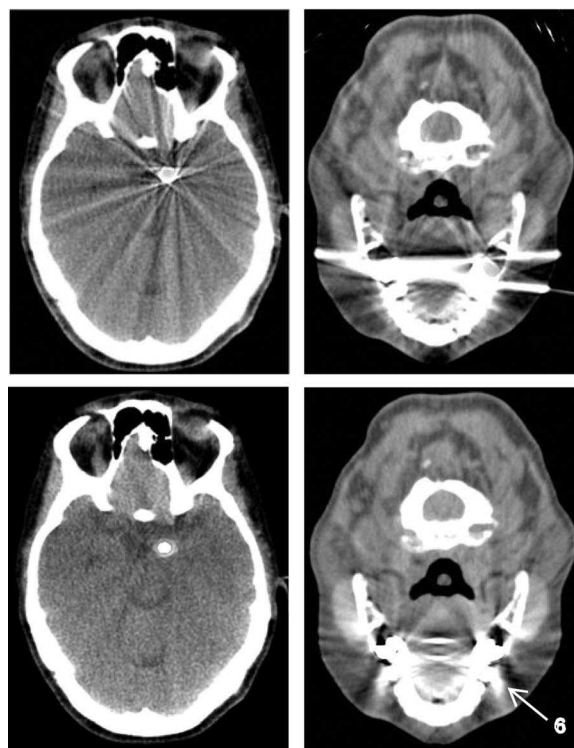


FIG. 12. Images reconstructed with ratio interpolation. The priors for the top row images were thresholded DI-MAR images (Fig. 9, row 3), and the priors for the bottom row images were from our proposed method. Along with Fig. 9, these images suggest that the prior is more critical than the interpolation technique. However, for multiple pieces of metal, the interpolation technique itself begins to play a role as seen by the degraded image quality of the right column compared to Fig. 9.

loss of some edge structure, especially if those structures are close to the metal pieces.

In order to study the impact of the interpolation technique relative to the accuracy of the prior, we also use the ratio interpolation with our prior and with the thresholded prior.⁶ This interpolation uses the ratio of scanner projections and reprojections, so that the reprojections themselves need not be substituted in the trace. This is a potential improvement on methods that directly use the reprojections in the metal trace, e. g.,⁵ because reprojections may themselves be inaccurate. The interpolation technique results are shown in Fig. 12. Comparing with the difference interpolation shown in Fig. 9, we see that in the case of a single metal object, the image quality of the difference interpolation and ratio interpolation methods is nearly the same when our prior was used. The image quality of the ratio interpolation image is nearly the same as the difference interpolation also when the thresholded prior was used. These two results indicate that the prior has greater impact than the particular interpolation method. Note that the ratio interpolation however only works well when the metal object is removed from the prior. The reason is the same one that we discuss in Sec. III, i. e., that beam hardening coupled with thresholding creates overestimated or underestimated reprojections. These reprojections are naturally consistent across view angles, but not once they are multiplied by the ratio of projections, which are not a constant unless the

reprojections exactly equal the scanner projections. Therefore, ratio interpolation works well for images with single metal objects, not those containing multiple ones. For multiple metal objects, the metals should not be left out of the prior, because while interpolating the trace of one metal piece, we must consider the interfering edges created by the second metal trace. If we leave them out, we miss edges and create secondary artifacts (arrow 6). Therefore, the interpolation method itself has an impact when there are multiple pieces of metal.

Metal objects that are close together will have traces that overlap in more views than objects that are far apart. For this reason, we recommend that the metal thresholds be lowered, or the metal objects dilated, to reduce possible high frequency secondary artifacts resulting from one metal trace abruptly entering and leaving another trace. However, for metal objects that are close together, we are likely to get some secondary artifacts because we do not correctly quantify the metal pieces themselves. We saw evidence of this error in case 2 in Fig. 9. There is also a blurry region around each piece of metal resulting from the smoothing of data in the spline fit. All MAR algorithms in the literature exhibit similar blurring. A non-linear correction for reduction of discontinuity may be helpful. In cases 4 and 8, the separation of bone from artifact using a one-parameter curve was imperfect. This is because of the interference between the four metal pieces, which makes the distance-intensity relationship deviate from the exponential form we see with smaller or fewer pieces. Also due to interference, the artifacts were as bright as the metal edges, and were not excluded by thresholding. For these reasons, the image quality of case 8 is not as good as the other cases. The image quality from the other methods is poor too because the metal pieces are large, close together, and embedded in dense anatomical structures.

VI.B. Limitations of this research and future work

One of the limitations of this research is that we have tested our algorithm only on head images. Optimization and testing of our algorithm for head images was considered to be of high impact due to the clinical importance of head CTs, subtle differences in normal and abnormal findings, and the frequent occurrence of metal artifacts. We have set the parameters at each stage based on CT values of anatomical tissue, air, and metal. We have also tested the algorithm steps within ranges of parameter values to reduce the risks of overfitting. However, the parameters (or the criteria to choose them) may need examination or adjustment for other anatomical regions, and further studies to assess the performance of our algorithm on those regions are needed.

Another concern is the robustness of the algorithm in the presence of different implants or more pieces of metal. Our data set was limited. The cases we tested had endovascular coils, deep-brain stimulators, and dental fillings. These comprise the common metal implants in head CT images at our facility. More pieces will lead to more complicated interference patterns. We have seen that when multiple pieces of metal are close together (as in case 8), the clusters in the

intensity-distance relationship are not as well extracted by a single-parameter exponential as they are when there are fewer pieces. Multiple rounds of cluster identification or a superposition of discrimination curves may be required in such cases. In future work, a higher dimensional hypersurface may be investigated, involving the gradient and other predictors of artifacts, for better discrimination of bright artifacts from bone. Consideration of gradient amplitude and phase might help in removing the residual bright artifact in the prior for the dental image.

A third limitation is that if noise due to photon starvation is the dominant artifact, our method is unlikely to work. However, images from modern CT scanners are not usually limited by photon starvation. These scanners have more powerful x-ray tubes and use a variety of modulation techniques to obtain enough power (photon counts) to reduce noise while limiting dose. In addition, adaptive filtering is applied in the scanners to reduce noise to acceptable levels.¹⁵

In future work, we can add to the prior knowledge to build a more accurate prior image. An anatomical atlas may help distinguish between anatomy and artifact. An instance of where an atlas may have been useful is case 8. The residual bright artifact in the soft tissue between the teeth in the prior for the dental image could be identified as unlikely to be anatomical. Machine learning techniques could potentially be useful classifying the labels as artifacts or anatomy. There is much potential for exploration of computer vision and learning algorithms in developing a prior image.

VII. CONCLUSION

Metal artifacts are predictable because phenomena such as beam hardening that cause them are well understood. We have made some observations about the appearance of metal artifacts and used these to segment the metal artifacts from anatomical structures. We have used the results of the segmentation to build up a prior knowledge image that guides the data replacement step for an effective metal artifact reduction. We have tested this concept of using image segmentation and artifact predictability to discriminate artifacts from anatomy on head images. The priors resulting from our method produce better quality images than DI-MAR or priors obtained from thresholding other images. We have found that an accurate prior knowledge image has more impact on final image quality than the choice of a particular interpolation technique.

ACKNOWLEDGMENTS

The authors thank Dr. Xiaoqian Jiang for helpful discussions on clustering. This work was sponsored by the Lawrence Livermore National Laboratories and the Department of Homeland Security Science and Technology Directorate.

APPENDIX A: CONTOURING THE OUTER BOUNDARY

We create a closed contour along the outer boundary of the anatomy in the original image, shown by the broken line

in Fig. 6(a). The contour is assigned a low value of soft tissue such as $I_t = -100$ HU. The contour must be at least two voxels thick to prevent the later steps from removing it.

There are many contour tracking algorithms which would work for this simple contour generation problem; we have used an algorithm that thresholds the image, and then connects outer boundary pixels with 8-connectivity. We use a threshold of -600 HU, which is well below soft-tissue intensities, to account for tissue corrupted by artifacts. If there are multiple disconnected objects in the image, and hence multiple contours, we keep only the largest one.

APPENDIX B: CORRECTION OF ERRORS FROM ARTIFACT REGION REPLACEMENT

OBR and CBR replace regions of voxels with single values. If left this way, the prior image would be “patchy,” and the final image would have the appearance of patchy texture. To avoid this, voxel values between the limits of I_t and I_{\min} are replaced with the mode value of the original image. This range includes most soft tissue, but the exact limits are not critical, and the range can be made larger. Soft tissue variations will be removed from the prior. The soft tissue variations do not contribute to secondary artifacts, and it is better to replace them, to avoid patchiness from CBR and OBR. The data replacement method, described below, does not substitute the scanner projections with the reprojections of the prior, so the soft tissue details are not lost.

APPENDIX C: REPLACEMENT OF SINOGRAM DATA

The prior [shown in Fig. 6(f)] is then reprojected, and the metal trace is found in the reprojections by calculation of the rays passing through the metal image. We have used the method described in Ref. 3 for data replacement. In this method, the reprojections are subtracted from the scanner projections. The difference projections are smoother than the scanner projections. The interpolation of metal traces is done on the difference projections and the interpolated result is added to the reprojections to create the final corrected projections that are then reconstructed to create the final image. We modify this interpolation method in that we fit a second order spline to five samples on both sides of the metal trace instead of using linear interpolation. Linear interpolation of two samples should not be relied upon because sampling errors and noise will result in poor estimates of data.

^{a)} Author to whom correspondence should be addressed. Electronic mail: seemeen.karimi@gmail.com

¹ G. Glover and N. Pelc, “An algorithm for reduction of metal clip artifacts in CT reconstructions,” *Med. Phys.* **8**, 799–807 (1981).

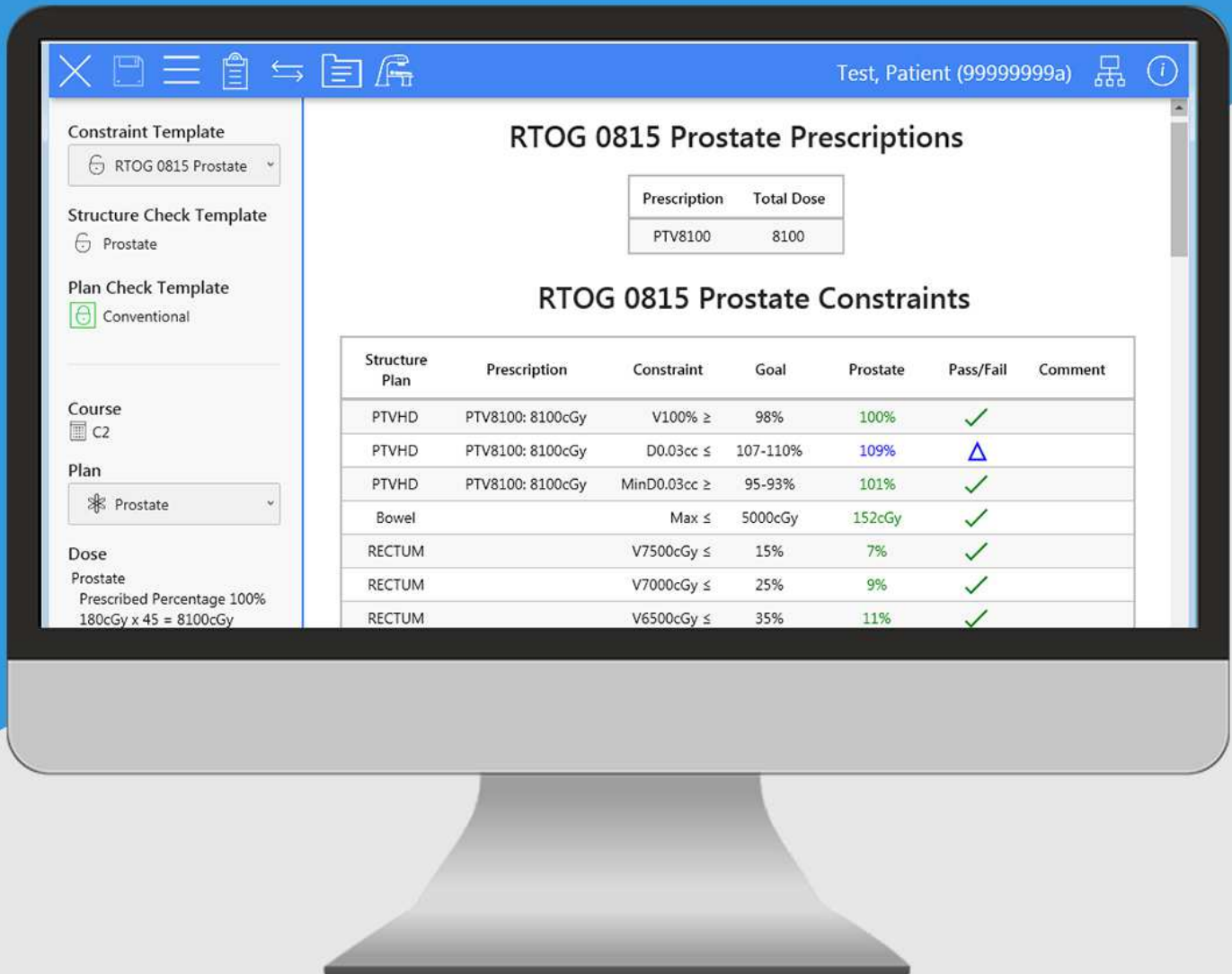
² W. Kalender, R. Hebel, and J. Ebersberger, “Reduction of CT artifacts caused by metallic implants,” *Radiology* **164**, 576–577 (1987).

³ R. Naidu, I. Bechwati, S. Karimi, S. Simanovsky, and C. Crawford, “Method of and system for reducing metal artifacts in images generated by x-ray scanning devices,” U.S. patent 6,721,387 (13 April 2004).

- ⁴ H. Li, L. Yu, X. Liu, J. Fletcher, and C. McCollough, “Metal artifact suppression from reformatted projections in multislice helical CT using dual front active contours,” *Med. Phys.* **37**, 5155–5164 (2010).
- ⁵ M. Bal and L. Spies, “Metal artifact reduction in CT using tissue-class modeling and adaptive filtering,” *Med. Phys.* **33**, 2852–2859 (2006).
- ⁶ E. Meyer, R. Raupach, M. Lell, B. Schmidt, and M. Kachelries, “Normalized metal artifact reduction (NMAR) in Computed tomography,” *Med. Phys.* **37**, 5482–5493 (2010).
- ⁷ S. Mazin and N. Pelc, “Metal Artifact Reduction Algorithm for X-Ray CT Using a Three-Pass Approach,” *AAPM 51st Annual Meeting*, Anaheim, CA, edited by C. Serago and D. Pfeiffer, 2009.
- ⁸ F. E. Boas and D. Fleischmann, “Evaluation of two iterative techniques for reducing metal artifacts in computed tomography,” *Radiology* **259**(3), 894–902 (2011).
- ⁹ W. Veldkamp, R. Joemai, A. van der Molen, and J. Geleijns, “Development and validation of segmentation and interpolation for metal artifact suppression,” *Med. Phys.* **37**, 620–628 (2010).
- ¹⁰ R. Joemai, P. W. de Bruin, W. Veldkamp, and J. Geleijns, “Metal artifact reduction for CT: Development, implementation, and clinical comparison of a generic and a scanner-specific technique,” *Med. Phys.* **39**, 1125–1132 (2012).
- ¹¹ H. Y. Yu, K. Zeng, D. K. Bharkhada, G. Wang, M. T. Madsen, O. Saba, B. Policeni, M. A. Howard, and W. R. K. Smoker, “A segmentation-based method for metal artifact reduction,” *Acad. Radiol.* **14**, 495–504 (2007).
- ¹² J. Verbarg and J. Seco, “CT metal artifact reduction method correcting for beam hardening and missing projections,” *Phys. Med. Biol.* **57**, 2803–2818 (2012).
- ¹³ E. Meyer, R. Raupach, M. Lell, B. Schmidt, and M. Kachelries, “Frequency split metal artifact reduction (FSMAR) in computed tomography,” *Med. Phys.* **39**, 1904–1916 (2012).
- ¹⁴ B. De Man, J. Nuyts, P. Dupont, G. Marchal, and P. Suetens, “Metal streak artifacts in x-ray computed tomography: A simulation study,” *IEEE Trans. Nucl. Sci.* **46**, 691–696 (1999).
- ¹⁵ H. Hsieh, “Adaptive streak artifact reduction in computed tomography resulting from excessive x-ray photon noise,” *Med. Phys.* **25**, 2137–2149 (1998).
- ¹⁶ C. Lai, “Streak suppression filter for use in computed tomography systems,” U.S. patent 5,680,426 (21 October 1997).
- ¹⁷ X. Zhang and J. Wang, “Metal artifact reduction in x-ray computed tomography by constrained optimization,” *Med. Phys.* **38**, 701–711 (2011).
- ¹⁸ B. deMan et al., “Reduction of metal streak artifacts in x-ray CT using a transmission MAP algorithm,” *IEEE Trans. Nucl. Sci.* **47**, 997–981 (2000).
- ¹⁹ G. Wang, T. Frei, and M. Vannier, “Fast iterative algorithm for metal artifact reduction in x-ray CT,” *Acad. Radiol.* **7**(8), 607–614 (2000).
- ²⁰ R. E. Alvarez and A. Macovski, “Energy selective reconstructions in x-ray computed tomography,” *Phys. Med. Biol.* **21**, 733–744 (1976).
- ²¹ J. A. Fessler, I. Elbakri, P. Sukovic, and N. H. Clinthorne, “Maximum-likelihood dual-energy tomographic image reconstruction,” *Proc. SPIE. Medical Imaging: Image Processing* **4684**, 38–49 (2002).
- ²² F. Bamberg, A. Dierks, K. Nikolaou, M. Reiser, C. Becker, and T. Johnson, “Metal artifact reduction by dual energy CT using monoenergetic extrapolation,” *Eur. Radiol.* **21**, 1424–1429 (2011).
- ²³ A. Kak and M. Slaney, *Principles of Computerized Tomographic Imaging* (IEEE, 1998).
- ²⁴ J. Hsieh, *Computed Tomography, Principles, Design, Artifacts and Recent Advances* (SPIE, Bellingham, 2002).
- ²⁵ P. Joseph and R. Spital, “A method for correcting bone-induced artifacts in computed tomography scanners,” *J. Comput. Assist. Tomogr.* **2**, 100–108 (1978).
- ²⁶ E. de Paula, “XSPEC, Center for Instrumentation, Dosimetry and Radiation Protection (CIDRA),” 1984.
- ²⁷ M. J. Berger and J. H. Hubbell, XCOM: Photon Cross Sections on a Personal Computer, Center for Radiation Research, National Bureau of Standards, 1987.
- ²⁸ R. Gonzalez, R. Woods, and S. Eddins, *Digital Image Processing using MATLAB*, 2nd ed. (Gatesmark Publishing, 2009).

ClearCheck

One-click plan evaluation



Dose Constraints • Plan Checks
Structure Checks • Collision Checks